ACS APPLIED MATERIALS & INTERFACES

www.acsami.org

Research Article

Zincblende $InAs_xP_{1-x}$/InP Quantum Dot Nanowires for Telecom Wavelength Emission

Giada Bucci,* Valentina Zannier, Francesca Rossi, Anna Musiał, Jakub Boniecki, Grzegorz Sęk, and Lucia Sorba

Cite This: *ACS Appl. Mater. Interfaces* 2024, 16, 26491−26499

Read Online

ACCESS | Metrics & More | Article Recommendations

ABSTRACT: $InAs_xP_{1-x}$ quantum dots (QDs) in InP nanowires (NWs) have been realized as a platform for emission at telecom wavelengths. These QDs are typically grown in NWs with the wurtzite crystal phase, but in this case, ultrathin diameters are required to achieve defect-free heterostructures, making the structures less robust. In this work, we demonstrate the growth of pure zincblende $InAs_xP_{1-x}$ QDs in InP NWs, which enabled an increase in NW diameters to about 45 nm, achieved by employing Au-assisted vapor liquid solid growth in a chemical beam epitaxy system. We studied the growth of InP/$InAs_xP_{1-x}$ heterostructures with different compositions to control the straight growth along the ⟨100⟩ direction and to tune the emission wavelength. Interestingly, we found that the growth mechanism for pure InAs QDs is different compared to that for $InAs_xP_{1-x}$ alloy QDs. This allowed us to optimize different growth protocols to achieve straight growth of the final QD NWs. We successfully obtained the growth of $InAs_xP_{1-x}$ QDs with a composition in the range of x = 0.24−1.00. By means of microphotoluminescence measurements, we demonstrate the tunability of the emission in dependence of the $InAs_xP_{1-x}$ QD composition and morphology, remarkably observing an emission at the telecom O-band for a 10 nm thick QD with 80% of As content.

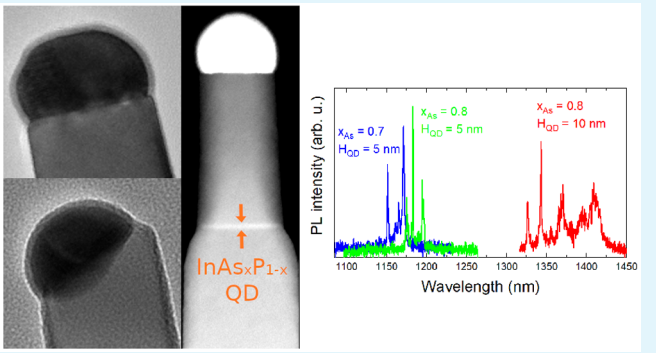

KEYWORDS: *nanowires, quantum dots, telecom emission, InAsP/InP heterostructures, vapor−liquid−solid growth*

1. INTRODUCTION

Semiconductor quantum dots (QDs) are an interesting platform with possible applications in quantum information technologies based on optics,[1−4] because they can be used to realize single-photon sources (SPSs). In particular, SPSs at telecom bands are interesting for ultrasecure quantum optical communication using existing fiber networks, because at these wavelengths there is a minimum for the losses and the dispersion in telecommunication fibers.[5,6] Indeed, semiconductor QDs have been proven as efficient sources in the telecom band,[7−12] emitting on-demand high-purity single and indistinguishable photons or even polarization-entangled photon pairs.[13−16] Many crucial milestones concerning application of QD-based devices in secure quantum information technology have been reported, including sources with high efficiency of single-photon emission,[17−20] operation at elevated temperatures,[1,21,22] integration with a silicon platform,[23] deterministic fabrication of QD structures,[24] and fully integrated, fiber-coupled QD-based sources of single photons,[25] including demonstration of quantum communication schemes.[26] In the last 2 decades, the realization of SPSs emitting at the telecom band has also been demonstrated in semiconductor QDs epitaxially grown in nanowires (NWs).[27,28] The exploitation of NW QDs has some important advantages compared to other types of QDs (such as Stranski−Krastanov QDs): (i) the growth mechanism of heterostructured NWs forming the QD leads to the possibility to control and tune QD features like QD dimensions, crystal phase,[29] composition, and density; (ii) semiconductor NWs open up the possibility to also grow highly lattice-mismatched heterostructures as a result of the relaxation of the elastic strain in the radial direction;[30] (iii) vapor−liquid−solid (VLS) growth of the NWs makes it possible to control the position in which the QDs are grown, both on the substrate and along the axis of the NW, opening up the possibility to grow coupled QDs in the same NW, which are naturally aligned along the NW axis;[31,32] and (iv) it is possible to epitaxially grow a

Received: January 11, 2024
Revised: March 13, 2024
Accepted: March 13, 2024
Published: May 10, 2024

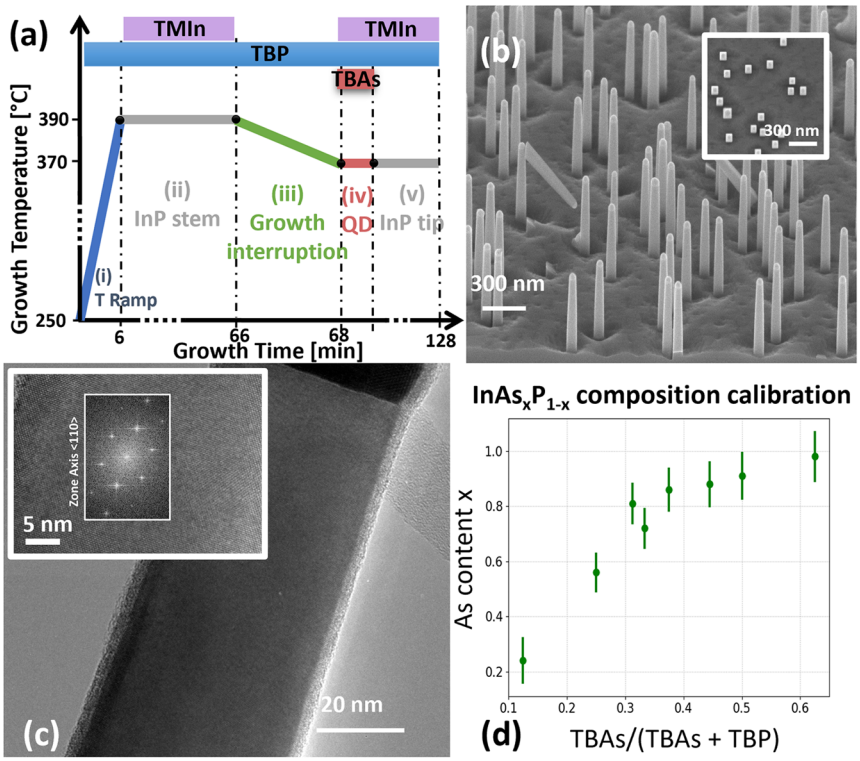

Figure 1. (a) Growth protocol exploited for the growth of the QD NWs. On the axes, the values are out of scale. (b) SEM 45° side-view image of InP NW stems grown along the ⟨100⟩ direction. In the inset, a top-view SEM image of the same sample. (c) HRTEM image of an InP NW near the catalyst nanoparticle (which is the dark region at the top of the figure). In the inset, a magnification of the NW with its fast Fourier transform in the ⟨110⟩ zone axis is shown. (d) Calibration curve of the $InAs_xP_{1-x}$ segment composition in dependence of the TBAs partial pressure.

waveguide directly around the QD, realizing what has been commonly called a "nanowire antenna" and increasing the extraction efficiency of the emitter.[33]

Among the possible heterostructures explored in the literature for telecom emission, $InAs_xP_{1-x}$ QDs in InP NWs have been investigated. Commonly, these QDs are grown along the ⟨111⟩ direction in ultrathin wurtzite (WZ) InP NWs, with a low As content in the ternary alloy ($x \sim 0.25$), and they have demonstrated single-photon ground state emission at $\lambda \sim$ 950 nm.[34−41] Recently, emission in the telecom O and C bands has also been demonstrated by varying the QD thickness and increasing the As content incorporated in the QD.[39,42] However, increasing the As content makes the growth of the heterostructure more challenging. In fact, phenomena such as kinking[43] and downward growth[44] have been observed for alternating InP and InAs segments in Au-assisted NWs. To the best of our knowledge, the growth of the $InAs_xP_{1-x}$ ternary alloy in InP NWs has been reported only in the ⟨111⟩ direction. Also, pure InAs/InP axial heterostructures have been investigated in the ⟨111⟩ direction with a WZ crystal phase and mainly in InAs NWs.[45−47] Besides the material choice and QD dimensions, it has been shown that the crystal phase purity is a crucial parameter for the emitters because the presence of stacking faults is highly detrimental to the QD emission. In particular, stacking faults can act as charge traps that confine charges along the NW axis but let them free perpendicularly, creating a varying electrostatic environment of the QD and leading to a significant broadening of the emission lines via so-called spectral diffusion[35,38] as well as decreased coherence time and indistinguishability of emitted photons. InP NWs grown along the ⟨111⟩ direction have shown a pure WZ crystal phase only for very thin diameters of 20 nm or less and by properly choosing the growth conditions.[48,49] In fact, along the ⟨111⟩ direction, the stacking fault formation during the NW growth is very easy because the energy difference between the WZ and zincblende (ZB) stacking sequence is quite small, with an energy barrier for the WZ/ZB transition of ∼3.4 meV/atom in InP NWs along the ⟨111⟩ direction with diameters larger than 20 nm.[50] Conversely, NWs grown along the ⟨100⟩ direction show a pure ZB crystal phase for a wide range of diameters and growth conditions,[51] because the only stable staking sequence in the ⟨100⟩ direction is the ZB.[52−54] The constraint to have such a small diameter in the WZ NWs leads to less flexibility in the tunability of the QD dimension and to a more difficult manipulation and fabrication of such ultrathin NWs. For these reasons, the possibility to grow a QD in NWs with larger diameters is important to simplify the post-growth processing.

In this work, we realize $InAs_xP_{1-x}$ QDs in pure ZB InP NWs grown along the ⟨100⟩ direction. Different compositions and QD dimensions are explored, demonstrating the tunability of these emitters, which is confirmed in high-resolution photoluminescence (PL) measurements. They revealed clearly single QD spectra at low temperatures, which for the NWs with higher As contents and larger QD thickness could be tuned through 1.3 μm of the second telecom window. These results open up a way for fabricating a new class of quantum emitters with high potential for their application as sources of single photons or more complex photonic states to be employed in some of the schemes in quantum communication in the fiber networks or quantum computing.

https://doi.org/10.1021/acsami.4c00615
ACS Appl. Mater. Interfaces 2024, 16, 26491−26499

2. MATERIALS AND METHODS

All of the NWs in this work are synthesized by means of Au-assisted VLS growth in a Riber C-21 chemical beam epitaxy (CBE) system on InP(100) substrates. Trimethylindium (TMIn), *tert*-butyl arsine (TBAs), and *tert*-butyl phosphine (TBP) are used as gaseous metal−organic precursors, for which it is possible to measure the line pressures as a reference for the fluxes introduced into the chamber. The substrate temperature is measured with a pyrometer and cross-checked with the manipulator thermocouple, providing an overall accuracy of ±10 °C. Before the substrate is mounted inside the CBE chamber, gold catalyst nanoparticles are deposited from the colloidal dispersion. Commercial water solutions of Au colloids with a nominal diameter of 30 nm (BBInternational EM.GCnn) are employed. InP(100) substrates are first dipped for 30 s in a 0.1% poly-L-lysine solution, rinsed in deionized (DI) water, and blown dry under N_2 flux. The colloidal solution is drop-casted on the substrate surface, which is then rinsed in DI water and blown dry.

After the growth, the samples are imaged exploiting scanning electron microscopy (Zeiss Merlin SEM) operating at 5 kV. The samples are imaged from both the top and side views with a tilting angle of 45° to check the NW morphology and dimensions.

Transmission electron microscopy (TEM) analysis is carried out using two microscopes: a JEOL JEM-2200FS, equipped with an in-column Ω filter operated at 200 kV, and a high-resolution FEG TEM JEOL JEM-F200. For these measurements, we used QD NWs grown in identical growth conditions as those investigated by micro-photoluminescence (μ-PL) but with a shorter InP tip (maximum length around 100 nm). The short InP tip is necessary to check the crystal quality and the QD thicknesses.

The alloy composition is measured through energy-dispersive X-ray analysis (EDX) employing a Bruker Quantax EDS system mounted on a Zeiss Ultraplus SEM.

All of the geometrical parameters of the NWs and QDs are measured via the image analysis software ImageJ.

Emission measurements from single NWs with QDs are performed using a μ-PL setup with high spectral (20 μeV) and spatial (2 μm) resolution optimized for the near-infrared spectral range. The NWs are excited non-resonantly above E_g of InP (typically with 640 nm line of a semiconductor continuous-wave laser diode). A long working distance (20 mm) infinity-corrected microscope objective with a numerical aperture of 0.4 focused the laser beam on the sample surface and collected the QD emission. The detection system consists of a monochromator (1 m focal length for the highest resolution experiments) and a nitrogen-cooled multichannel InGaAs linear array photodetector. The sample is mounted on a coldfinger of a liquid helium continuous-flow optical cryostat, which allows for tuning and controlling the temperature. All of the samples are pre-characterized by measuring emission from the ensembles of as-grown NWs, and then μ-PL from selected single NWs is measured on NWs mechanically transferred on Si(111) substrates, patterned with Au markers for spatial orientation on the sample surface. Markers are prepared by optical lithography using a MicroWriter ML3 system. Gold is deposited through thermal evaporation and then lifted off.

3. RESULTS AND DISCUSSION

3.1. InP Stem and $InAs_xP_{1-x}$ Composition Calibration. The growth of the QD NWs is conducted following a similar protocol, which is schematized in Figure 1a: (i) A first ramp from the standby temperature (~250 °C) to the InP stem growth temperature T_{stem} = 390 ± 10 °C under a TBP line pressure of 1 Torr is conducted. (ii) TMIn is introduced inside the chamber to start the growth of the InP stem for 60 min, employing TMIn and TBP line pressures of 0.4 and 0.65 Torr, respectively. (iii) A growth interruption of 2 min and 30 s is done to prepare the proper TBP and TBAs line pressures and to adjust the growth temperature for the $InAs_xP_{1-x}$ QD growth. During the growth interruption, TMIn flux is interrupted and the sample is maintained under a TBP flux only, which is ramped from its initial value of 0.65 Torr to the line pressure providing the selected QD alloy composition. In fact, as it will be discussed later, several compositions have been explored in this work, leading to the choice of different line pressures for TBP and TBAs. (iv) The QD is grown by introducing TMIn and TBAs again in the chamber, with a composition given by the selected fluxes, while the duration of the QD growth determines its thickness (height). (v) An InP tip is axially grown for 60 min at the same temperature of the QD and employing TMIn and TBP line pressures of 0.4 and 1.0 Torr, respectively.

In Figure 1b, a SEM image of the InP NW stem ensemble obtained at the end of step (ii) is shown from a side view with a tilt angle of 45°. The average top NW diameter is D_{stem} = 48 ± 4 nm. The growth conditions chosen for the stem result in a high yield of vertical InP NWs grown along the ⟨100⟩ direction (~93% of the NWs). The remaining NWs grow along different growth directions, which have already been observed and investigated in the literature for InP NWs grown on (100)-oriented substrates.[55] The chosen growth conditions also lead to a non-negligible radial growth of InP, resulting in a slightly tapered NW morphology. In the inset of Figure 1b, a top-view SEM image of the same sample shows that all of the NWs have a square cross section, a fingerprint of the underlying ZB crystal structure. In Figure 1c, a HRTEM image of an InP stem NW is shown, along with a magnified image with its fast Fourier transform (FFT) in the ⟨110⟩ zone axis in the inset. The FFT demonstrates the pure ZB crystal phase of our InP stems.

We focus now on the growth of the ternary alloy segment of $InAs_xP_{1-x}$ on the InP stem at 370 °C, employing steps (iii) and (iv) of the growth protocol. To investigate the tunability of the $InAs_xP_{1-x}$ composition, several $InAs_xP_{1-x}$ segments are grown using different precursor line pressures and measured by EDX. Figure 1d reports a calibration curve of the As content in the $InAs_xP_{1-x}$ segment as a function of the TBAs partial pressure. By choosing the proper TBAs and TBP line pressures, we were able to grow ternary alloy segments with an x index ranging from 0.24 ± 0.08 to 1.00 (pure InAs). However, the growth of straight $InAs_xP_{1-x}$ segments on the InP stem presents several challenges. In the next section, the optimization of the growth protocol during the growth interruption, i.e., for the switch from InP to $InAs_xP_{1-x}$, is discussed more in detail.

3.2. $InAs_xP_{1-x}$ Growth Mechanism. Dependent upon the ternary alloy composition, different growth parameters play a crucial role during the growth of the heterostructure. Interestingly, a different behavior is found between the ternary alloys $InAs_xP_{1-x}$ with an x index value of up to 0.91 ± 0.08 and pure InAs (x = 1.00).

Concerning the $InAs_xP_{1-x}$ segment, as mentioned before, a growth interruption is mandatory to prepare and stabilize the chosen TBAs and TBP line pressures for the growth of the QD. However, the growth interruption seems to deeply affect the growth mechanism of the $InAs_xP_{1-x}$ segment, as visible in Figure 2. Panel (a) shows a schematic of the two growth protocols explored for the switch from InP to $InAs_xP_{1-x}$, with two different growth interruptions indicated as GI 1 and GI 2. GI 1 is a growth interruption during which the growth temperature is constant, TMIn flux is interrupted, and TBP line flux is ramped from its stem value to the value employed for the $InAs_xP_{1-x}$ growth. GI 2 is conducted exactly like GI 1 but decreasing the temperature by 20 °C. In both cases, an $InAs_xP_{1-x}$ segment with an 88% As content is grown right after

https://doi.org/10.1021/acsami.4c00615
ACS Appl. Mater. Interfaces 2024, 16, 26491−26499

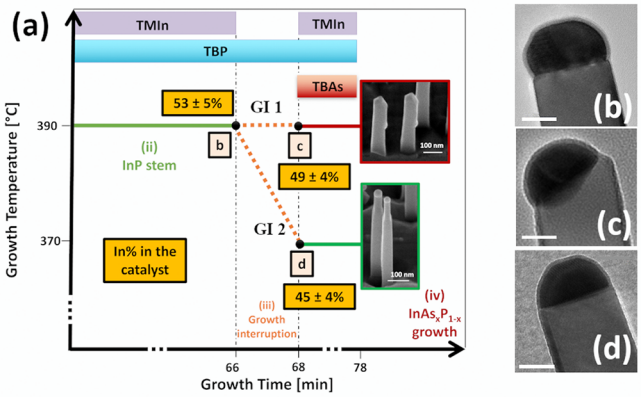

Figure 2. (a) Growth protocol schemes exploited for the study of the growth mechanisms. On the axes, the values are out of scale. (b) TEM image of the catalyst droplet right before the growth interruption, indicated as point "b" in the schematic in panel a. (c) TEM image of the catalyst droplet right after the growth interruption GI 1 and before the $InAs_xP_{1-x}$ growth, indicated as point "c" in the schematic in panel a. (d) TEM image of the catalyst droplet right after the growth interruption GI 2 and before the $InAs_xP_{1-x}$ growth, indicated as point "d" in the schematic in panel a. The scale bar for panels b–d is 20 nm.

the growth interruption. We found that, after GI 1 in 94% of the NWs, a downward growth is observed, while after GI 2, mainly all of the NWs (95%) show a straight morphology of the $InAs_xP_{1-x}$ segment, as shown in the SEM images reported in the red and green insets, respectively. Similar results are obtained for $InAs_xP_{1-x}$ segments with a lower As composition. Therefore, we might conclude that it is possible to grow a straight $InAs_xP_{1-x}$ segment only by decreasing the temperature during the growth interruption.

To understand what is the effect of the growth interruption on the catalyst nanoparticle, we measured by EDX–TEM the composition of the nanoparticles right before the growth interruption (point "b" in Figure 2a) and right after the two different growth interruptions GI 1 and GI 2 (points "c" and "d" in Figure 2a, respectively). To ensure that the catalyst composition analyzed at TEM is the same as that during the growth, the samples are cooled after the growth without any flux in the ultra-high vacuum (UHV) chamber, as demonstrated in ref 56.

We found that, in both cases, the effect of the growth interruption is a small reduction of the In content inside the catalyst from a value of 53 ± 5% to a lower value (see the exact percentages in the orange boxes in Figure 2a). The In content in the catalyst after GI 1 and GI 2 is, however, similar. Thus, we can conclude that the In variation itself, from InP growth to $InAs_xP_{1-x}$ growth, is not the parameter responsible for the resulting growth mode of the $InAs_xP_{1-x}$ segment.

Figure 2 also reports the TEM images of the catalyst before the growth interruption (panel b), right after the growth interruption GI 1 (panel c), and right after GI 2 (panel d). After GI 1, 98% of the NWs show a non-straight interface between the InP stem and the catalyst, while after GI 2, 100% of the NWs in the sample have a straight interface. A similar dependence of the NW/catalyst interface stability in the temperature window of the growth interruption has already been observed in the literature in InP NWs grown along the ⟨111⟩ direction.[57] It has been reported that interrupting group III flux at a high temperature and low group V flux causes the unpinning of the catalyst droplet from the top of the NW and lets the catalyst slide down toward the NW sidewalls. This unpinning process has been attributed to a reduction in the supersaturation of the catalyst as a result of the high temperature/low P flux conditions during the growth interruption. This favors the creation of a truncated area at the NW top, which facilitates the catalyst droplet to wet the NW sidewalls. Finally, when the growth is started again, the unstable configuration of the catalyst determines epitaxial growth of the new solid phase along the NW facets, resulting in a downward growth mode. A similar mechanism may also happen in our case for GI 1, because it is conducted at the same high temperature as the InP stem growth, decreasing P flux. On the contrary, with the decrease of the growth temperature during the growth interruption, i.e., performing GI 2, the catalyst stays stable on the NW top facet (Figure 2d) and the result is a straight interface. Thus, we can conclude that $InAs_xP_{1-x}$ grows straight as long as the interface between the catalyst and the InP NW remains flat after the growth interruption, like in Figure 2d, and this is mainly determined by the growth temperature rather than the In content of the catalyst. We observe this behavior for all of the $InAs_xP_{1-x}$ compositions explored in this work, except for pure InAs.

In fact, if the same successful growth strategy of GI 2 is exploited for the growth of pure InAs QD on the InP stem, the InAs segment does not grow straight. Figure 3a shows a SEM

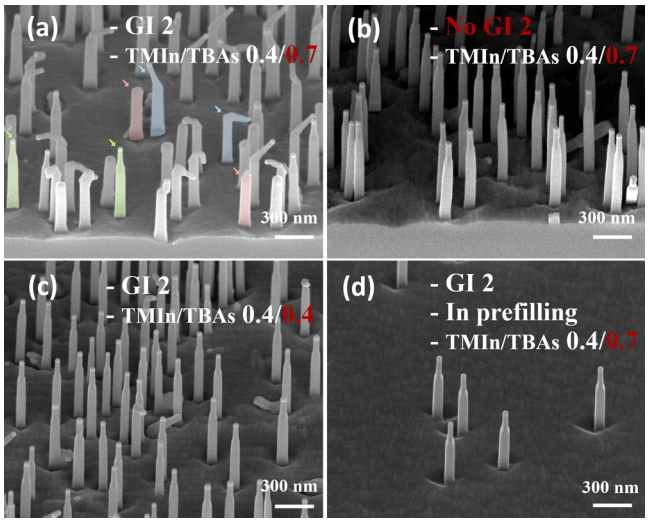

Figure 3. SEM side-view images of InP NW stems followed by an InAs segment grown with different growth protocols: (a) by employing GI 2 with TMIn and TBAs at 0.4 and 0.7 Torr, respectively, with examples of kinked, straight, and downward grown NWs highlighted in blue, green, and red, respectively, (b) without GI 2 and employing TMIn and TBAs at 0.4 and 0.7 Torr, respectively, (c) by employing GI 2 and TMIn and TBAs both at 0.4 Torr, and (d) by employing GI 2 followed by In catalyst prefilling and TMIn and TBAs at 0.4 and 0.7 Torr, respectively.

image of a sample grown employing GI 2 followed by 10 min of InAs growth with TMIn and TBAs line pressures of 0.4 and 0.7 Torr, respectively. In this sample, three different NW morphologies are present: a low percentage of straight NWs highlighted in green in the image (~8%), a major percentage of kinked NWs highlighted in blue (~57%), and downward grown NWs highlighted in red (~35%). As demonstrated in Figure 2d, by employing GI 2, the interface between the catalyst and the InP stem is maintained flat after the growth

https://doi.org/10.1021/acsami.4c00615
ACS Appl. Mater. Interfaces 2024, 16, 26491–26499

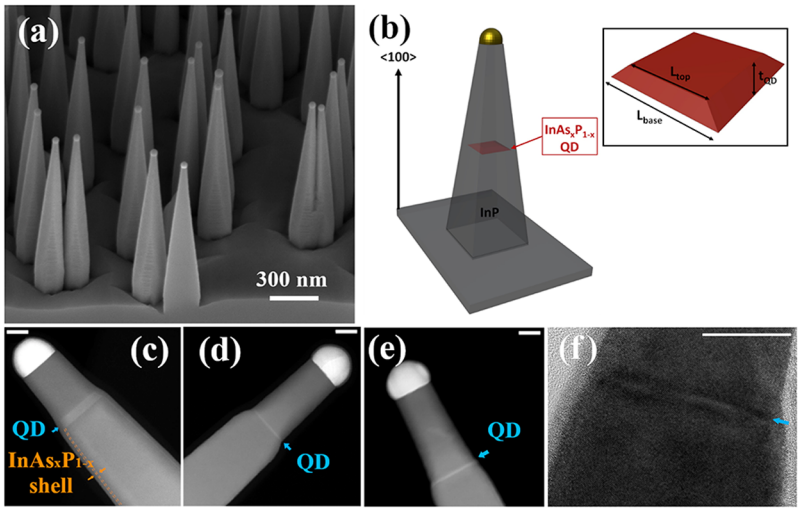

Figure 4. (a) SEM side-view image of a 10 nm thick $InAs_{0.88}P_{0.12}$ QD. (b) Schematic of the geometry of emitters grown in this work, with an $InAs_xP_{1-x}$ QD embedded in an InP NW. In the inset, the truncated pyramid shape of the QD is shown. (c) STEM image of $InAs_{0.88}P_{0.12}$ of 10 nm thickness (highlighted with a blue arrow). (d) STEM image of a 3 nm thick $InAs_{0.88}P_{0.12}$ QD. (e) STEM image of a 3 nm thick InAs QD. (f) TEM image of the 3 nm thick InAs QD. The scale bar for panels c−f is 20 nm.

interruption. Thus, the non-straight InAs growth might be explained by some instability occurring at the early stage of the InAs growth after GI 2. We found that it is possible to obtain straight InAs growth on the InP stem by employing three different growth protocols: (i) by avoiding the growth interruption and directly growing InAs at the end of the InP growth, with TMIn and TBAs line pressures of 0.4 and 0.7 Torr, respectively, (ii) by keeping the growth interruption GI 2 but reducing the As flux for the InAs growth, i.e., using both TMIn and TBAs line pressures of 0.4 Torr, and (iii) by employing an In prefilling of the catalyst for 30 s after GI 2 and subsequently growing InAs with TMIn and TBAs line pressures of 0.4 and 0.7 Torr, respectively. SEM images of the samples grown with these successful protocols are shown in panels b, c, and d of Figure 3, respectively, where the improvement of the straight growth mode compared to the sample in Figure 3a is evident. These three growth protocols have in common a higher amount of In in the catalyst droplet at the beginning of InAs growth compared to the sample after GI 2 (45 ± 4% In), which gives a non-straight growth (Figure 3a). In fact, without any GI, the catalyst nanoparticles have 53 ± 5% In and the InAs segment grows straight (Figure 3b). The sample in Figure 3c is grown with a lower V/III pressure ratio; therefore, the nanoparticles have a higher In content.[58] Lastly, for the sample of Figure 3d, we exploit an In prefilling of the catalyst droplet before InAs growth, increasing the In content after GI 2 and resulting in straight growth. We thus believe that the main requirement for the straight growth of pure InAs on InP is that the In content inside the catalyst must be high. A similar behavior has already been reported for the growth of InAs at the top of GaAs NWs along the ⟨111⟩ direction[45] and in the switch from InP to InAs in InAs/InP heterostructure NWs along the ⟨111⟩ direction.[46] We speculate that the higher amount of In in the catalyst nanoparticle leads to the straight growth of InAs because it increases the catalyst droplet contact angle, satisfying the condition required by the system to be in the stability window for the straight growth.[45] The conditions, which apply for InAs, are not required for $InAs_xP_{1-x}$ probably because of the different surface energies of the two materials, affecting in a different way the nanoparticle stability conditions.

3.3. $InAs_xP_{1-x}$ QD NW Growth and Optical Measurements. Thus far, we have demonstrated that it is possible to grow straight $InAs_xP_{1-x}$ segments on InP NWs grown along the ⟨100⟩ direction with a composition ranging from $x = 0.24$ to pure InAs. In this section, we focus on the $InAs_xP_{1-x}$ QDs and show their optical emission as a function of the QD composition and dimension, as deduced from the structural characterization.

In Figure 4a, a SEM image of the $InAs_{0.88}P_{0.12}$ QD NWs with a QD of 10 nm thickness is presented. It is possible to observe that, during the axial growth of the InP tip after the QD, also a significant radial growth of the material around the QD occurs, resulting in tapered NWs. This radial growth of InP also ensures the passivation of the QD. In Figure 4b, a schematic of the $InAs_xP_{1-x}$ QD embedded in the InP NW is shown. Because the NWs have a square cross section, the QD shape is that of a truncated pyramid. It is worth mentioning that the top side length of the pyramid is a bit smaller than the base side length in this case because the alloy catalyst shrinks during the $InAs_xP_{1-x}$ QD growth. This happens probably because of the reduction of the In content in the catalyst compared to the InP stem value and, thus, a reduction of the catalyst volume. A schematic of the QD shape is shown in the inset of Figure 4b. The truncated pyramid has in all of our samples typically a major base side length of $L_{base} \sim 55$ nm and a minor top side length of $L_{top} \sim 45$ nm.

In Figure 4c, a scanning transmission electron microscopy (STEM) image of a 10 nm thick $InAs_{0.88}P_{0.12}$ QD is reported, of which the position is highlighted with a blue arrow. Interestingly, it is possible to observe the presence of an $InAs_xP_{1-x}$ shell (highlighted with orange lines) of 1−2 nm thickness, which is a result of the radial growth of $InAs_xP_{1-x}$ simultaneously occurring during QD axial growth. This parasitic radial growth has never been reported for the same kind of heterostructures in the ⟨111⟩ direction with a WZ crystal phase,[34−41] except for ref 47, in which, however, it is localized near the QD and does not extend all over the NW stem length. On the contrary, it has been often reported in ZB NW heterostructures.[59] An $InAs_xP_{1-x}$ shell can generate unpredictable effects and can potentially be detrimental to

https://doi.org/10.1021/acsami.4c00615
ACS Appl. Mater. Interfaces 2024, 16, 26491−26499

the QD emission in terms of both line broadening and intensity. The wave functions of the carriers confined in the QD can partly leak out into the shell, making them more sensitive to the surface states acting as non-radiative recombination centers and carrier loss channels. As a result of the same reasons, the QD excitons can be more exposed to fluctuations of the charges on the NW sidewalls. This would contribute to increased broadening of the emission lines as a result of the spectral diffusion effect, in a similar way to other types of charge traps as the crystal defects in the QD vicinity,[28,38] also commonly observed for other types of QDs.[60] Because the radial growth rate of this shell is much smaller than the QD axial growth rate, it is possible to avoid the shell by growing QDs with a smaller thickness of ∼2−4 nm. In Figure 4d, a STEM image of a 3 nm thick $InAs_{0.88}P_{0.12}$ QD is reported, where no $InAs_xP_{1-x}$ shell is visible. We also found that, for InAs QDs, the growth of 2−3 nm thick QD ensures that no InAs radial shell is visible at STEM nor at EDX, because it is possible to observe in Figure 4e where a 3 nm thick InAs QD STEM image is reported.

In Figure 4f, a TEM image shows the absence of structural defects around the QD, which is a common feature of all of the QD NW samples grown for this work.

The optical characterization of the QDs is performed by employing PL measurements. As already mentioned above, a preliminary characterization is performed on the ensembles of as-grown NWs to follow the main spectral changes caused by modifications in the growth conditions and NW morphology. These measurements include the contribution from more than one QD, because it is difficult to isolate a single standing NW in the as-grown ensemble, and it is not reported here. Thus, to appreciate the emission from a single QD, in the next step, μ-PL has been measured on single NWs mechanically transferred on a Si(111) substrate pre-patterned with gold markers. Figure 5 shows such single NW spectra to mainly illustrate the effect of the changed QD thickness (t_{QD}) and the nominal QD material composition (arsenic content of x). Figure 5a shows three spectra for $x = 0.70$ with QD thickness of $t_{QD} = 5$ nm and for $x = 0.80$ with QD thickness of $t_{QD} = 5$ and 10 nm. What is mainly observed is the spectral shifts as expected, i.e., both increasing the As content or the QD thickness red shifting the emission: in the first case as a result of the red shift of the QD material bandgap energy and in the second case as a result of quantum size effects. It is worth underlining that, for arsenic content of 80% and QD thickness of about 10 nm, the emission reaches the second telecom O-band window and even enters the extended E band, exhibiting the potential of these nanostructures for nanophotonic applications. Figure 5b shows analogous examples but for the samples with thinner $InAs_xP_{1-x}$ QDs, i.e., those for which the $InAs_xP_{1-x}$ shell is not expected and not observed in the STEM images. Here, similar spectral tuning of the single QD lines can be observed from slightly above 1.1 μm to about 1.3 μm of the second telecom window, which could be obtained by employing larger As contents up to pure InAs QD material. For pure InAs, the O-band emission can be reached for 2-fold thinner QDs with a thickness in the range of 4 nm, providing stronger energy quantization and, therefore, better isolation of single QD states and related optical transitions. In the case of presented spectra, the dominant role of spectral diffusion effects on the emission line width is visible, with a typical line broadening on the order of hundreds of microelectronvolts, exceeding by far the spectral resolution of the experimental setup (20 μeV).

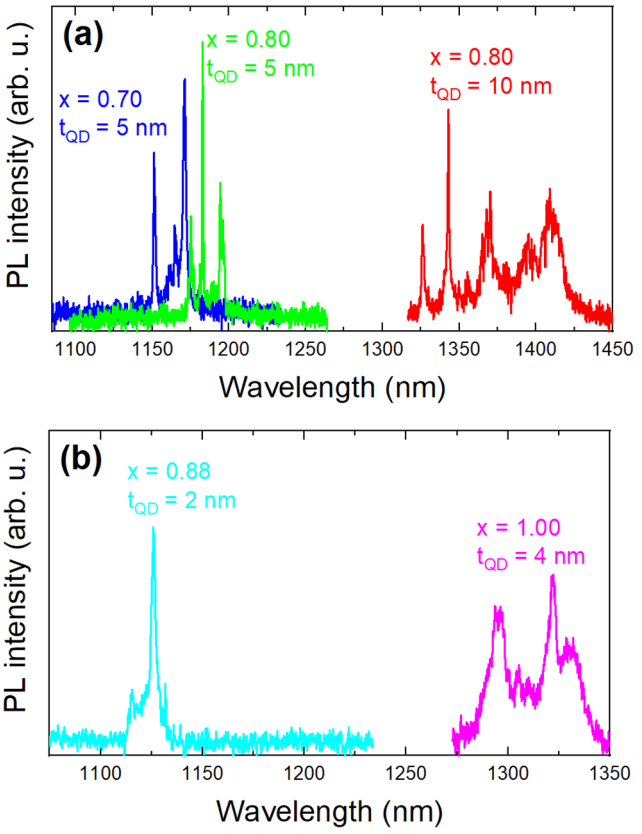

Figure 5. μ-PL spectra at 4 K of single-QD NWs with (a) As content of $x = 0.70$ and 5 nm thickness (blue), $x = 0.80$ and 5 nm thickness (green), and $x = 0.80$ and 10 nm thickness (red) and (b) $x = 0.88$ and 2 nm of thickness (light blue) and $x = 1.00$ and 4 nm of thickness (pink).

Finally, it needs to be mentioned that a single QD spectrum consists of a few emission lines, even for the lowest excitation powers. This has already been observed especially for dots characterized by large dimensions, similar to those in our case.[61−63] They can originate from either emission of other excitonic complexes (like biexciton or charged complexes) or exciton excited states. Detailed analysis of the origin of the lines is beyond the scope of this work, but in comparison to reports from the literature concerning QDs of similar sizes in an InP-based material system, both are possible for the emission line separation detected for QDs investigated here; see, e.g., ref 64.

4. CONCLUSION

In summary, we have successfully optimized the growth of $InAs_xP_{1-x}$ QDs in InP NWs grown along the ⟨100⟩ direction and with a pure ZB crystal structure, with a ternary alloy composition spanning from $x = 0.24$ to 1.00 and QD thicknesses from 2 to 10 nm. We studied the optimal growth conditions to fabricate straight InP/$InAs_xP_{1-x}$ heterostructures, observing a different behavior between InP/$InAs_xP_{1-x}$ and InP/InAs. We successfully demonstrated the tunability of the emission of QDs depending upon the QD composition and thickness. Remarkably, QDs with 80% of As and 10 nm of thickness demonstrate emission in the telecom O- and even E-bands.

https://doi.org/10.1021/acsami.4c00615
ACS Appl. Mater. Interfaces 2024, 16, 26491−26499

AUTHOR INFORMATION

Corresponding Author

Giada Bucci − *NEST Istituto Nanoscienze Consiglio Nazionale delle Ricerche (CNR) and Scuola Normale Superiore, 56127 Pisa, Italy;* orcid.org/0000-0003-0372-690X; Email: giada.bucci@sns.it

Authors

Valentina Zannier − *NEST Istituto Nanoscienze Consiglio Nazionale delle Ricerche (CNR) and Scuola Normale Superiore, 56127 Pisa, Italy;* orcid.org/0000-0002-9709-5207

Francesca Rossi − *Istituto dei Materiali per l'Elettronica ed il Magnetismo (IMEM)−Consiglio Nazionale delle Ricerche (CNR), 43124 Parma, Italy;* orcid.org/0000-0003-1773-2542

Anna Musiał − *Department of Experimental Physics, Wrocław University of Science and Technology, 50-370 Wrocław, Poland;* orcid.org/0000-0001-9602-8929

Jakub Boniecki − *Department of Experimental Physics, Wrocław University of Science and Technology, 50-370 Wrocław, Poland*

Grzegorz Sęk − *Department of Experimental Physics, Wrocław University of Science and Technology, 50-370 Wrocław, Poland*

Lucia Sorba − *NEST Istituto Nanoscienze Consiglio Nazionale delle Ricerche (CNR) and Scuola Normale Superiore, 56127 Pisa, Italy;* orcid.org/0000-0001-6242-9417

Complete contact information is available at: https://pubs.acs.org/10.1021/acsami.4c00615

Author Contributions

Giada Bucci, Valentina Zannier, and Lucia Sorba have performed the growth of the NWs and the growth mechanism study. Francesca Rossi carried out the TEM analysis. Anna Musiał, Grzegorz Sęk, and Jakub Boniecki performed the optical studies of the QD NWs. The manuscript is written through contributions of all authors. All authors have given approval to the final version of the manuscript.

Notes

The authors declare no competing financial interest.

ACKNOWLEDGMENTS

Valentina Zannier acknowledges financial support from the PRIN Project 20223WZ245-GROUNDS, "Growth and Optical Studies of Tunable Quantum Dots and Superlattices in Semiconductor Nanowires". Giada Bucci acknowledges the financial support provided by the European COST Action OPERA (CA-20116) through the short-term scientific mission program. The authors acknowledge the Center for Instrument Sharing of the University of Pisa (CISUP) for the TEM facilities.

ABBREVIATIONS USED

CBE, chemical beam epitaxy; EDX, energy-dispersive X-ray analysis; FFT, fast Fourier transform; GI 1, growth interruption 1; GI 2, growth interruption 2; HRTEM, high-resolution transmission electron microscopy; NW, nanowire; PL, photoluminescence; QD, quantum dot; SEM, scanning electron microscopy; SPS, single-photon source; TBAs, *tert*-butyl arsine; TBP, *tert*-butyl phosphine; TEM, transmission electron microscopy; TMIn, trimethylindium; VLS, vapor−liquid−solid; WZ, wurtzite; ZB, zincblende; μ-PL, micro-photoluminescence

REFERENCES

(1) Arakawa, Y.; Holmes, M. J. Progress in Quantum-Dot Single Photon Sources for Quantum Information Technologies: A Broad Spectrum Overview. *Appl. Phys. Rev.* **2020**, *7* (2), No. 021309.

(2) Knill, E.; Laflamme, R.; Milburn, G. J. A Scheme for Efficient Quantum Computation with Linear Optics. *Nature* **2001**, *409* (6816), 46−52.

(3) Fattal, D.; Diamanti, E.; Inoue, K.; Yamamoto, Y. Quantum Teleportation with a Quantum Dot Single Photon Source. *Phys. Rev. Lett.* **2004**, *92* (3), 37904.

(4) Michler, P. Quantum Dots for Quantum Information Technologies. In *Nano-Optics and Nanophotonics*; Michler, P., Ed.; Springer International Publishing: Cham, Switzerland, 2017; DOI: 10.1007/978-3-319-56378-7.

(5) Cao, X.; Zopf, M.; Ding, F. Telecom Wavelength Single Photon Sources. *J. Semicond.* **2019**, *40* (7), No. 071901.

(6) Benyoucef, M.; Musiał, A. Telecom Wavelengths InP-Based Quantum Dots for Quantum Communication. In *Photonic Quantum Technologies*; Benyoucef, M., Ed.; Wiley: Hoboken, NJ, 2023; Chapter 18, pp 463−507, DOI: 10.1002/9783527837427.ch18.

(7) Schwertberger, R.; Gold, D.; Reithmaier, J. P.; Forchel, A. Long-Wavelength InP-Based Quantum-Dash Lasers. *IEEE Photonics Technol. Lett.* **2002**, *14* (6), 735−737.

(8) Wang, B.; Zhao, F.; Peng, Y.; Jin, Z.; Li, Y.; Liu, S. Self-Organized InAs Quantum Dots Formation by As/P Exchange Reaction on (001) InP Substrate. *Appl. Phys. Lett.* **1998**, *72* (19), 2433−2435.

(9) Folliot, H.; Loualiche, S.; Lambert, B.; Drouot, V.; Le Corre, A. Effects of Interface-Layers Composition and Strain Distribution on the Optical Transitions of InAs Quantum Dots on InP. *Phys. Rev. B* **1998**, *58* (16), 10700−10704.

(10) Zhukov, A. E.; Ustinov, V. M.; Egorov, A. Y.; Kovsh, A. R.; Zaitsev, S. V.; Gordeev, N. Y.; Kopchatov, V. I.; Ledentsov, N. N.; Tsatsul'nikov, A. F.; Volovik, B. V.; Kop'ev, P. S.; Alferov, Z. I. Low-Threshold Quantum Dot Injection Laser Emitting at 1.9 μm. *Proceedings of the 10th Conference on Semiconducting and Insulating Materials (SIMC-X) (Cat. No.98CH36159)*; Berkeley, CA, June 1−5, 1998; pp 319−322,.

(11) Fafard, S.; Wasilewski, Z.; McCaffrey, J.; Raymond, S.; Charbonneau, S. InAs Self-Assembled Quantum Dots on InP by Molecular Beam Epitaxy. *Appl. Phys. Lett.* **1996**, *68* (7), 991−993.

(12) Leonelli, R.; Tran, C. A.; Brebner, J. L.; Graham, J. T.; Tabti, R.; Masut, R. A.; Charbonneau, S. Optical and Structural Properties of Metalorganic-Vapor-Phase-Epitaxy-Grown InAs Quantum Wells and Quantum Dots in InP. *Phys. Rev. B* **1993**, *48* (15), 11135−11143.

(13) Olbrich, F.; Höschele, J.; Müller, M.; Kettler, J.; Luca Portalupi, S.; Paul, M.; Jetter, M.; Michler, P. Polarization-Entangled Photons from an InGaAs-Based Quantum Dot Emitting in the Telecom C-Band. *Appl. Phys. Lett.* **2017**, *111* (13), 133106.

(14) Zeuner, K. D.; Jöns, K. D.; Schweickert, L.; Reuterskiöld Hedlund, C.; Nuñez Lobato, C.; Lettner, T.; Wang, K.; Gyger, S.; Schöll, E.; Steinhauer, S.; Hammar, M.; Zwiller, V. On-Demand Generation of Entangled Photon Pairs in the Telecom C-Band with InAs Quantum Dots. *ACS Photonics* **2021**, *8* (8), 2337−2344.

(15) Nawrath, C.; Olbrich, F.; Paul, M.; Portalupi, S. L.; Jetter, M.; Michler, P. Coherence and Indistinguishability of Highly Pure Single Photons from Non-Resonantly and Resonantly Excited Telecom C-Band Quantum Dots. *Appl. Phys. Lett.* **2019**, *115* (2), 023103.

(16) Ward, M. B.; Karimov, O. Z.; Unitt, D. C.; Yuan, Z. L.; See, P.; Gevaux, D. G.; Shields, A. J.; Atkinson, P.; Ritchie, D. A. On-Demand Single-Photon Source for 1.3 μm Telecom Fiber. *Appl. Phys. Lett.* **2005**, *86* (20), 201111.

(17) Senellart, P.; Solomon, G.; White, A. High-Performance Semiconductor Quantum-Dot Single-Photon Sources. *Nat. Nanotechnol* **2017**, *12* (11), 1026−1039.
(18) Holewa, P.; Sakanas, A.; Gür, U. M.; Mrowiński, P.; Huck, A.; Wang, B.-Y.; Musiał, A.; Yvind, K.; Gregersen, N.; Syperek, M.; Semenova, E. Bright Quantum Dot Single-Photon Emitters at Telecom Bands Heterogeneously Integrated on Si. *ACS Photonics* **2022**, *9* (7), 2273−2279.
(19) Musiał, A.; Mikulicz, M.; Mrowiński, P.; Zielińska, A.; Sitarek, P.; Wyborski, P.; Kuniej, M.; Reithmaier, J. P.; Sęk, G.; Benyoucef, M. InP-Based Single-Photon Sources Operating at Telecom C-Band with Increased Extraction Efficiency. *Appl. Phys. Lett.* **2021**, *118* (22), 221101.
(20) Liu, S.; Srinivasan, K.; Liu, J. Nanoscale Positioning Approaches for Integrating Single Solid-State Quantum Emitters with Photonic Nanostructures. *Laser Photon Rev.* **2021**, *15* (10), 2100223.
(21) Dusanowski, Ł.; Syperek, M.; Misiewicz, J.; Somers, A.; Höfling, S.; Kamp, M.; Reithmaier, J. P.; Sęk, G. Single-Photon Emission of InAs/InP Quantum Dashes at 1.55 μ m and Temperatures up to 80 K. *Appl. Phys. Lett.* **2016**, *108* (16), 163108.
(22) Olbrich, F.; Kettler, J.; Bayerbach, M.; Paul, M.; Höschele, J.; Portalupi, S. L.; Jetter, M.; Michler, P. Temperature-Dependent Properties of Single Long-Wavelength InGaAs Quantum Dots Embedded in a Strain Reducing Layer. *J. Appl. Phys.* **2017**, *121* (18), 184302.
(23) Elshaari, A. W.; Pernice, W.; Srinivasan, K.; Benson, O.; Zwiller, V. Hybrid Integrated Quantum Photonic Circuits. *Nat. Photonics* **2020**, *14* (5), 285−298.
(24) Rodt, S.; Reitzenstein, S.; Heindel, T. Deterministically Fabricated Solid-State Quantum-Light Sources. *J. Phys.: Condens. Matter* **2020**, *32* (15), No. 153003.
(25) Musiał, A.; Żołnacz, K.; Srocka, N.; Kravets, O.; Große, J.; Olszewski, J.; Poturaj, K.; Wójcik, G.; Mergo, P.; Dybka, K.; Dyrkacz, M.; Dłubek, M.; Lauritsen, K.; Bülter, A.; Schneider, P.; Zschiedrich, L.; Burger, S.; Rodt, S.; Urbańczyk, W.; Sęk, G.; Reitzenstein, S. Plug&Play Fiber-Coupled 73 kHz Single-Photon Source Operating in the Telecom O-Band. *Adv. Quantum Technol.* **2020**, *3* (6), 2000018.
(26) Gao, T.; Rickert, L.; Urban, F.; Große, J.; Srocka, N.; Rodt, S.; Musiał, A.; Żołnacz, K.; Mergo, P.; Dybka, K.; Urbańczyk, W.; Sęk, G.; Burger, S.; Reitzenstein, S.; Heindel, T. A Quantum Key Distribution Testbed Using a Plug&Play Telecom-Wavelength Single-Photon Source. *Appl. Phys. Rev.* **2022**, *9* (1), 011412.
(27) Laferriére, P.; Haffouz, S.; Northeast, D. B.; Poole, P. J.; Williams, R. L.; Dalacu, D. Position-Controlled Telecom Single Photon Emitters Operating at Elevated Temperatures. *Nano Lett.* **2023**, *23* (3), 962−968.
(28) Dalacu, D.; Poole, P. J.; Williams, R. L. Nanowire-Based Sources of Non-Classical Light. *Nanotechnology* **2019**, *30* (23), No. 232001.
(29) Lozano, M. S.; Gómez, V. J. Epitaxial Growth of Crystal Phase Quantum Dots in III−V Semiconductor Nanowires. *Nanoscale Adv.* **2023**, *5* (7), 1890−1909.
(30) Larsson, M. W.; Wagner, J. B.; Wallin, M.; Håkansson, P.; Fröberg, L. E.; Samuelson, L.; Wallenberg, L. R. Strain Mapping in Free-Standing Heterostructured Wurtzite InAs/InP Nanowires. *Nanotechnology* **2007**, *18* (1), No. 015504.
(31) Phoenix, J.; Korkusinski, M.; Dalacu, D.; Poole, P. J.; Zawadzki, P.; Studenikin, S.; Williams, R. L.; Sachrajda, A. S.; Gaudreau, L. Magnetic Tuning of Tunnel Coupling between InAsP Double Quantum Dots in InP Nanowires. *Sci. Rep* **2022**, *12* (1), 5100.
(32) Tateno, K.; Zhang, G.; Gotoh, H.; Sogawa, T. VLS Growth of Alternating InAsP/InP Heterostructure Nanowires for Multiple-Quantum-Dot Structures. *Nano Lett.* **2012**, *12* (6), 2888−2893.
(33) Friedler, I.; Sauvan, C.; Hugonin, J. P.; Lalanne, P.; Claudon, J.; Gérard, J. M. Solid-State Single Photon Sources: The Nanowire Antenna. *Opt Express* **2009**, *17* (4), 2095−2110.
(34) Dalacu, D.; Mnaymneh, K.; Wu, X.; Lapointe, J.; Aers, G. C.; Poole, P. J.; Williams, R. L. Selective-Area Vapor−Liquid−Solid Growth of Tunable InAsP Quantum Dots in Nanowires. *Appl. Phys. Lett.* **2011**, *98* (25), 251101.
(35) Dalacu, D.; Mnaymneh, K.; Lapointe, J.; Wu, X.; Poole, P. J.; Bulgarini, G.; Zwiller, V.; Reimer, M. E. Ultraclean Emission from InAsP Quantum Dots in Defect-Free Wurtzite InP Nanowires. *Nano Lett.* **2012**, *12* (11), 5919−5923.
(36) Versteegh, M. A. M.; Reimer, M. E.; Jöns, K. D.; Dalacu, D.; Poole, P. J.; Gulinatti, A.; Giudice, A.; Zwiller, V. Observation of Strongly Entangled Photon Pairs from a Nanowire Quantum Dot. *Nat. Commun.* **2014**, *5* (1), 5298.
(37) Huber, T.; Predojević, A.; Khoshnegar, M.; Dalacu, D.; Poole, P. J.; Majedi, H.; Weihs, G. Polarization Entangled Photons from Quantum Dots Embedded in Nanowires. *Nano Lett.* **2014**, *14* (12), 7107−7114.
(38) Reimer, M. E.; Bulgarini, G.; Fognini, A.; Heeres, R. W.; Witek, B. J.; Versteegh, M. A. M.; Rubino, A.; Braun, T.; Kamp, M.; Höfling, S.; Dalacu, D.; Lapointe, J.; Poole, P. J.; Zwiller, V. Overcoming Power Broadening of the Quantum Dot Emission in a Pure Wurtzite Nanowire. *Phys. Rev. B* **2016**, *93* (19), No. 195316.
(39) Haffouz, S.; Zeuner, K. D.; Dalacu, D.; Poole, P. J.; Lapointe, J.; Poitras, D.; Mnaymneh, K.; Wu, X.; Couillard, M.; Korkusinski, M.; Schöll, E.; Jöns, K. D.; Zwiller, V.; Williams, R. L. Bright Single InAsP Quantum Dots at Telecom Wavelengths in Position-Controlled InP Nanowires: The Role of the Photonic Waveguide. *Nano Lett.* **2018**, *18* (5), 3047−3052.
(40) Dalacu, D.; Poole, P. J.; Williams, R. L. Tailoring the Geometry of Bottom-Up Nanowires: Application to High Efficiency Single Photon Sources. *Nanomaterials* **2021**, *11* (5), 1201.
(41) Reimer, M. E.; Bulgarini, G.; Akopian, N.; Hocevar, M.; Bavinck, M. B.; Verheijen, M. A.; Bakkers, E. P. A. M.; Kouwenhoven, L. P.; Zwiller, V. Bright Single-Photon Sources in Bottom-up Tailored Nanowires. *Nat. Commun.* **2012**, *3* (1), 737.
(42) Wakileh, A. N.; Yu, L.; Dokuz, D.; Haffouz, S.; Wu, X.; Lapointe, J.; Northeast, D. B.; Williams, R. L.; Rotenberg, N.; Poole, P. J.; Dalacu, D. On-Demand Single Photon Emission in the Telecom C-Band from Nanowire-Based Quantum Dots. *arXiv.org, e-Print Arch., Quantum Phys.* **2023**, arXiv:2309.13381.
(43) Vlassov, S.; Oras, S.; Polyakov, B.; Butanovs, E.; Kyritsakis, A.; Zadin, V. Kinking in Semiconductor Nanowires: A Review. *Cryst. Growth Des* **2022**, *22* (1), 871−892.
(44) Gao, Q.; Tan, H. H.; Jackson, H. E.; Smith, L. M.; Yarrison-Rice, J. M.; Zou, J.; Jagadish, C. Growth and Properties of III−V Compound Semiconductor Heterostructure Nanowires. *Semicond. Sci. Technol.* **2011**, *26* (1), No. 014035.
(45) Zannier, V.; Ercolani, D.; Gomes, U. P.; David, J.; Gemmi, M.; Dubrovskii, V. G.; Sorba, L. Catalyst Composition Tuning: The Key for the Growth of Straight Axial Nanowire Heterostructures with Group III Interchange. *Nano Lett.* **2016**, *16* (11), 7183−7190.
(46) Fahlvik Svensson, S.; Jeppesen, S.; Thelander, C.; Samuelson, L.; Linke, H.; Dick, K. A. Control and Understanding of Kink Formation in InAs−InP Heterostructure Nanowires. *Nanotechnology* **2013**, *24* (34), No. 345601.
(47) Tchernycheva, M.; Cirlin, G. E.; Patriarche, G.; Travers, L.; Zwiller, V.; Perinetti, U.; Harmand, J.-C. Growth and Characterization of InP Nanowires with InAsP Insertions. *Nano Lett.* **2007**, *7* (6), 1500−1504.
(48) Paiman, S.; Gao, Q.; Tan, H. H.; Jagadish, C.; Pemasiri, K.; Montazeri, M.; Jackson, H. E.; Smith, L. M.; Yarrison-Rice, J. M.; Zhang, X.; Zou, J. The Effect of V/III Ratio and Catalyst Particle Size on the Crystal Structure and Optical Properties of InP. *Nanotechnology* **2009**, *20* (22), No. 225606.
(49) Johansson, J.; Dick, K. A.; Caroff, P.; Messing, M. E.; Bolinsson, J.; Deppert, K.; Samuelson, L. Diameter Dependence of the Wurtzite−Zinc Blende Transition in InAs Nanowires. *J. Phys. Chem. C* **2010**, *114* (9), 3837−3842.
(50) Chiaramonte, T.; Tizei, L. H. G.; Ugarte, D.; Cotta, M. A. Kinetic Effects in InP Nanowire Growth and Stacking Fault Formation: The Role of Interface Roughening. *Nano Lett.* **2011**, *11* (5), 1934−1940.

https://doi.org/10.1021/acsami.4c00615
ACS Appl. Mater. Interfaces 2024, 16, 26491−26499

(51) Battiato, S.; Wu, S.; Zannier, V.; Bertoni, A.; Goldoni, G.; Li, A.; Xiao, S.; Han, X. D.; Beltram, F.; Sorba, L.; Xu, X.; Rossella, F. Polychromatic Emission in a Wide Energy Range from InP-InAs-InP Multi-Shell Nanowires. *Nanotechnology* **2019**, *30* (19), No. 194004.
(52) Krishnamachari, U.; Borgstrom, M.; Ohlsson, B. J.; Panev, N.; Samuelson, L.; Seifert, W.; Larsson, M. W.; Wallenberg, L. R. Defect-Free InP Nanowires Grown in [001] Direction on InP (001). *Appl. Phys. Lett.* **2004**, *85* (11), 2077−2079.
(53) Cavalli, A.; Wang, J.; Esmaeil Zadeh, I.; Reimer, M. E.; Verheijen, M. A.; Soini, M.; Plissard, S. R.; Zwiller, V.; Haverkort, J. E. M.; Bakkers, E. P. A. M. High-Yield Growth and Characterization of ⟨100⟩ InP p−n Diode Nanowires. *Nano Lett.* **2016**, *16* (5), 3071−3077.
(54) Zhang, K.; Abbas, Y.; Jan, S. U.; Gao, L.; Ma, Y.; Mi, Z.; Liu, X.; Xuan, Y.; Gong, J. R. Selective Growth of Stacking Fault Free ⟨100⟩ Nanowires on a Polycrystalline Substrate for Energy Conversion Application. *ACS Appl. Mater. Interfaces* **2020**, *12* (15), 17676−17685.
(55) Fonseka, H. A.; Caroff, P.; Wong-Leung, J.; Ameruddin, A. S.; Tan, H. H.; Jagadish, C. Nanowires Grown on InP(100): Growth Directions, Facets, Crystal Structures, and Relative Yield Control. *ACS Nano* **2014**, *8* (7), 6945−6954.
(56) Zannier, V.; Rossi, F.; Dubrovskii, V. G.; Ercolani, D.; Battiato, S.; Sorba, L. Nanoparticle Stability in Axial InAs−InP Nanowire Heterostructures with Atomically Sharp Interfaces. *Nano Lett.* **2018**, *18* (1), 167−174.
(57) Kelrich, A.; Sorias, O.; Calahorra, Y.; Kauffmann, Y.; Gladstone, R.; Cohen, S.; Orenstein, M.; Ritter, D. InP Nanoflag Growth from a Nanowire Template by in Situ Catalyst Manipulation. *Nano Lett.* **2016**, *16* (4), 2837−2844.
(58) Zhang, Z.; Lu, Z.-Y.; Xu, H.-Y.; Chen, P.-P.; Lu, W.; Zou, J. Effect of V/III Ratio on the Structural Quality of InAs Nanowires. *Proceedings of the 2014 Conference on Optoelectronic and Microelectronic Materials & Devices*; Perth, Western Australia, Australia, Dec 14−17, 2014; pp 24−26,.
(59) Messing, M. E.; Wong-Leung, J.; Zanolli, Z.; Joyce, H. J.; Tan, H. H.; Gao, Q.; Wallenberg, L. R.; Johansson, J.; Jagadish, C. Growth of Straight InAs-on-GaAs Nanowire Heterostructures. *Nano Lett.* **2011**, *11* (9), 3899−3905.
(60) Abbarchi, M.; Troiani, F.; Mastrandrea, C.; Goldoni, G.; Kuroda, T.; Mano, T.; Sakoda, K.; Koguchi, N.; Sanguinetti, S.; Vinattieri, A.; Gurioli, M. Spectral Diffusion and Line Broadening in Single Self-Assembled GaAs/AlGaAs Quantum Dot Photoluminescence. *Appl. Phys. Lett.* **2008**, *93* (16), 162101.
(61) Gawełczyk, M.; Wyborski, P.; Podemski, P.; Reithmaier, J. P.; Höfling, S.; Sęk, G. Excited States of Neutral and Charged Excitons in Single Strongly Asymmetric InP-Based Nanostructures Emitting in the Telecom C Band. *Phys. Rev. B* **2019**, *100* (24), No. 241304.
(62) Holewa, P.; Kadkhodazadeh, S.; Gawełczyk, M.; Baluta, P.; Musiał, A.; Dubrovskii, V. G.; Syperek, M.; Semenova, E. Droplet Epitaxy Symmetric InAs/InP Quantum Dots for Quantum Emission in the Third Telecom Window: Morphology, Optical and Electronic Properties. *Nanophotonics* **2022**, *11* (8), 1515−1526.
(63) Wyborski, P.; Gawełczyk, M.; Podemski, P.; Wroński, P. A.; Pawlyta, M.; Gorantla, S.; Jabeen, F.; Höfling, S.; Sęk, G. Impact of MBE-Grown (In, Ga)As/GaAs Metamorphic Buffers on Excitonic and Optical Properties of Single Quantum Dots with Single-Photon Emission Tuned to the Telecom Range. *Phys. Rev. Appl.* **2023**, *20* (4), No. 044009.
(64) Zieliński, M. Excitonic Complexes in InAs/InP Nanowire Quantum Dots. *Phys. Rev. B* **2020**, *101* (19), No. 195302.

https://doi.org/10.1021/acsami.4c00615
ACS Appl. Mater. Interfaces 2024, 16, 26491−26499